



Abiogenic methanogenesis during experimental komatiite serpentinization: Implications for the evolution of the early Precambrian atmosphere

Codi Lazar^{a,*}, Thomas M. McCollom^b, Craig E. Manning^a

^a Department of Earth and Space Sciences, University of California at Los Angeles, Los Angeles CA 90095-1567, USA

^b CU Center for Astrobiology and Laboratory for Atmospheric and Space Physics, Campus Box 392, University of Colorado, Boulder CO 80309-0392, USA

ARTICLE INFO

Article history:

Received 6 March 2012

Received in revised form 27 July 2012

Accepted 28 July 2012

Available online 6 August 2012

Editor: J. Fein

Keywords:

Abiotic methanogenesis

Serpentinization

Precambrian atmosphere

Faint Young Sun problem

Fischer–Tropsch type synthesis

Komatiites

ABSTRACT

Hydrothermal alteration of oceanic ultramafic rocks can produce significant abiotic methane as a byproduct; however, the abundance of peridotites is limited in the modern basaltic oceanic crust. Abiogenic methanogenesis was likely more productive in the early Precambrian when komatiitic volcanism delivered a much larger proportion of ultramafic material to the crust. It is therefore possible that hydrothermal alteration in the Hadean and Archean could have led to a higher methane flux to the atmosphere than today, potentially influencing the average surface temperature of the early Earth. This hypothesis was tested in a series of experiments in which natural and synthetic komatiite powders were reacted with an aqueous solution containing isotopically labeled formic acid at 300 °C and 350 bars. Over 2 months, experiments containing the natural powder generated labeled methane (¹³CH₄) at a rate 5–8× faster than concurrent experiments containing the synthetic komatiite. A similar difference was also observed between the natural komatiite and previous experiments on olivine serpentinization at the same conditions. Faster rates of methanogenesis in the natural komatiite experiments could be due to catalysis by magnesiochromite, which was present only in the natural komatiites. However, this was ruled out because parallel experiments containing additional magnesiochromite failed to increase methane yields. The most likely catalysts of the remaining candidate minerals were deduced to be Ni-sulfides, common accessory minerals in komatiites that have previously been shown to accelerate organic reactions. Because Ni-sulfides were particularly abundant in Archean komatiites, the experiments imply that methane yields during seafloor alteration were higher on the early Earth than today. This inference, in combination with the assumptions of faster crustal production rates and greater volumetric proportions of ultramafic lithologies, leads to the conclusion that methane flux from serpentinization of an Archean komatiite-bearing oceanic crust was likely higher than that from metamorphism of the modern oceanic crust. Incorporation of this result into existing geodynamic and atmospheric models suggests that alteration of the Archean seafloor may have contributed to the regulation of temperature of the paleoatmosphere. However, additional sources of greenhouse gases are required to solve the Faint Young Sun paradox for the early Archean.

© 2012 Elsevier B.V. All rights reserved.

1. Introduction

Serpentinization is a hydrothermal metamorphic process restricted to ultramafic bulk compositions wherein olivine ± pyroxene reacts with water to form serpentine and associated minerals. Commonly, ferrous Fe in the reactant minerals oxidizes during the formation of magnetite and/or partially ferric lizardite (Evans, 2008). Redox equilibria between ferrous and ferric minerals can fix oxygen fugacity (*f*O₂) to such low values that H₂ becomes a significant component in the fluid (Frost, 1985; Evans, 2008). If oxidized carbon (e.g., bicarbonate or CO₂) is

present, methane may form abiotically via the idealized reaction (McCollom and Seewald, 2007):



Methane-bearing fluids with isotopic and chemical signatures consistent with an abiotic origin have been observed emanating from ultramafic-hosted springs on the seafloor (Charlou et al., 1998; Charlou et al., 2002; Kelley et al., 2005; McCollom and Seewald, 2007; Proskurowski et al., 2008). However, most of the oceanic crust is basaltic and most known submarine hydrothermal vents are basalt-hosted. Field observations (Charlou et al., 1996; Charlou et al., 2000) and theoretical calculations (Wetzel and Shock, 2000) show that methane concentrations are significantly lower in mafic-hosted hydrothermal systems than in ultramafic systems. Therefore, lithology is an important limitation on the abiotic methane flux from the modern oceanic crust. In contrast, the early Precambrian crust likely contained a larger fraction of ultramafic

* Corresponding author at: Geophysical Laboratory, Carnegie Institution of Washington, 5251 Broad Branch Rd. NW, Washington DC 20015, USA. Tel.: +1 202 478 8900; fax: +1 202 478 8901.

E-mail address: clazar@ciw.edu (C. Lazar).

rocks due to input from komatiitic volcanism (Arndt and Nisbet, 1982; Nisbet and Fowler, 1983; Arndt et al., 2008). Provided that there were adequate pathways for hydrothermal alteration of a komatiite-bearing crust, the oceanic flux of serpentinization-derived abiotic methane may have been greater during the early Precambrian than today.

Since CH₄ is a greenhouse gas, abiogenic methanogenesis via komatiite serpentinization may have influenced the average Precambrian atmospheric temperature (Kasting, 2005). Greenhouse gases have been proposed as a solution to the Faint Young Sun paradox, wherein geological evidence for a warm Archean atmosphere contradicts the icy surface temperatures predicted by standard astrophysical models of low solar luminosity (Kasting, 2005). Atmospheric methane may have contributed to an early Precambrian greenhouse effect, consistent with geological evidence that suggests a reduced early atmosphere (Pavlov et al., 2003). The source of this proposed methane has been an open question, but the expanding body of field, experimental, and theoretical evidence for abiogenic methanogenesis during alteration of ultramafic rocks strongly suggests that serpentinization of a komatiite-bearing oceanic crust may have played an important role.

Abiotic methanogenesis is sluggish at subseafloor conditions (Berndt et al., 1996; McCollom and Seewald, 2001), implying that the compositions of CH₄-bearing ultramafic hydrothermal fluids are kinetically controlled. Catalysis by transition metal-bearing accessory minerals known as Fischer–Tropsch-type (FTT) catalysts is thought to play an important role in hydrothermal abiotic methanogenesis (McCollom and Seewald, 2007). Enhanced CH₄ yields have been reported in experimental studies on synthetic endmember forms of Ni–Fe alloy, Fe-chromite (FeCr₂O₄), and pentlandite ((Ni,Fe)₉S₈) (Horita and Berndt, 1999; Foustoukos and Seyfried, 2004; Fu et al., 2008). In natural rocks, however, such catalysts are typically present only in trace abundance or absent altogether. Moreover, experiments on endmember compositions may not apply to the entire solid solution range of a given mineral.

The CH₄ flux from the Archean seafloor was recently estimated using data from modern peridotite-hosted springs (Emmanuel and Ague, 2007), but it is unclear whether the accessory phase assemblage of a modern serpentinite is analogous to that of a komatiite. No komatiite-hosted hydrothermal springs have yet been discovered, so comparing field measurements of komatiite-hosted and peridotite-hosted fluids is not possible. Therefore, we performed a series of hydrothermal methanogenesis experiments on natural and synthetic komatiites and compared the result to a previous olivine serpentinization experiment at identical conditions. Our results constrain the kinetic pathways for CH₄ production via

komatiite serpentinization and provide insight into the role of this CH₄ in an early Precambrian greenhouse atmosphere.

2. Methods

Bulk compositions of the starting solid materials are listed in Table 1. The natural komatiite, NAT1, was a cumulate peridotitic komatiite from the Abitibi greenstone belt. The sample was from the B3 knobby peridotite layer of the Pyke Hill complex near Munro Township, Ontario (Pyke et al., 1973; Arndt et al., 1977), and part of a komatiite petrographic suite from Western Minerals, Inc. Despite its 2.7 Ga age (Carignan et al., 1995), the prehnite–pumpellyite-grade (Arndt et al., 1977) Munro Township deposit experienced a lower degree of metamorphism than most other available komatiites, which are typically greenschist-grade or higher (Arndt and Nisbet, 1982).

The original petrographic description of major phases by Pyke et al. (1973) was confirmed via optical and electron microscopy, and powder X-ray diffraction (XRD). Major phases included unaltered olivine phenocrysts, spinifex clinopyroxene partially altered to tremolite, minor serpentine, and a partially devitrified glass matrix (Fig. 1A and B). All major XRD peaks could be explained by the presence of olivine, clinopyroxene, tremolite, and serpentine. A bulk chemical analysis was not performed on this particular rock, but may be approximated by the B3 analysis reported by Pyke et al. (Table 1) with the caveat that fractional crystallization effects during emplacement of the lava may have resulted in outcrop-scale modal heterogeneities. The field relationships between NAT1 and the B3 sample of Pyke et al. are unknown; thus, the B3 analysis is best viewed as an approximation of the NAT1 composition.

Backscattered electron (BSE) imaging of potentially catalytic accessory minerals in NAT1 showed minor magnetite, a 0.2–0.3% modal abundance of magnesiochromite, and a 0.2–0.3% modal abundance of bulk sulfides in the assembly chalcopyrite–pentlandite–sphalerite (Fig. 1C). The volumetric proportion of sulfide minerals was 60% chalcopyrite, 25% pentlandite, and 15% sphalerite, as estimated by point counting digital BSE images. Representative compositional analyses of the sulfides are presented in Table 3. Although pyrrhotite was reported in the petrographic description of the B3 layer by Pyke et al., it was not detected in the NAT1 sample.

The synthetic komatiite, SYN1, was constructed as a model ultramafic cumulate by mixing a glass with San Carlos olivine. Using the MELTS thermodynamic program (Ghiorso and Sack, 1995), the composition of the glass was calculated to be in equilibrium with olivine based on a starting

Table 1

Starting experimental powder compositions normalized to 100 wt.%. *Component masses of multi-ingredient powders are listed in Table 3. NAT1: approximated by the reported composition of the Pyke Hill B3 flow, Munro Township, 2.7 Ga Abitibi greenstone belt. NAT2: NAT1 plus Stillwater chromitite. SYN1: a model olivine cumulate composed of synthetic glass plus San Carlos olivine. SYN2: SYN1 plus Stillwater chromitite.

	NAT1 Munro ^a	NAT2* Munro + chromitite	SYN1* glass + olv	SYN2* glass + olv + chromitite	Stillwater magnesio-chromite ^b	Synthetic Glass ^b	San Carlos olivine ^b	Pyrolite ^c	MORB ^d
SiO ₂	41.0	33.6	48.3	39.9	4.2	50.8	40.9	42.9	49.3
Al ₂ O ₃	5.5	7.7	8.6	10.0	16.1	11.4	0.2	3.3	16.1
FeO	9.6	12.5	10.2	12.7	24	10.7	8.8	8.1	10.5
MgO	32.0	28.6	23.9	22.2	14.8	15.0	49.8	41.6	6.5
CaO	4.2	3.4	7.8	6.3	0.1	10.4	0.1	2.1	10.5
Na ₂ O	0.3	0.2	0.3	0.3	–	0.5	–	0.5	3.0
K ₂ O	0.1	0.1	0.1	0.1	–	0.1	–	0.2	0.1
TiO ₂	0.2	0.2	0.3	0.3	0.4	0.4	0.1	0.5	2.0
MnO	0.1	0.2	0.3	0.3	0.3	0.4	0.1	0.1	0.2
H ₂ O ⁺	5.5	4.4	–	–	–	–	–	0.2	0.7
H ₂ O [–]	0.7	0.6	–	–	–	–	–	–	1.0
CO ₂	0.4	0.3	–	–	–	–	–	–	–
Cr ₂ O ₃	0.4	8.3	0.2	7.8	40	0.3	–	0.5	<0.1

^a Pyke et al., 1973.

^b Electron microprobe analyses at UCLA.

^c Model mantle composition, Green and Ringwood, 1963.

^d Carmichael et al., 1974.

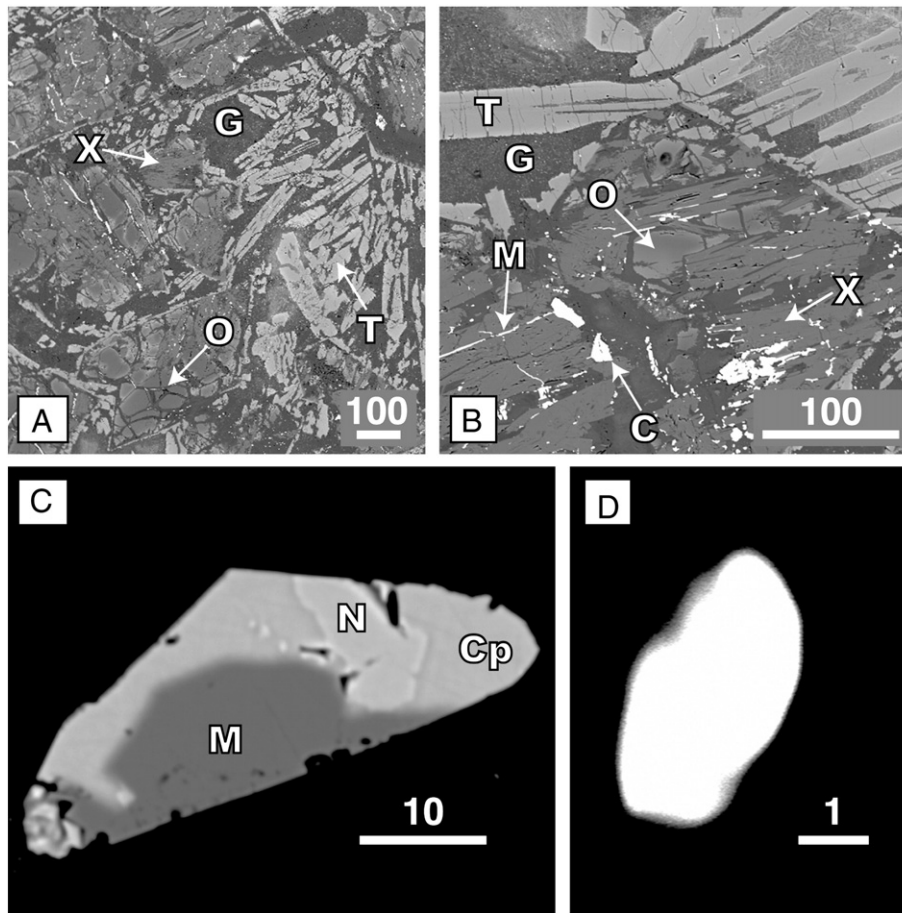


Fig. 1. Selected images of reactants and products. Scale bars in microns. A and B: Backscattered image of the Munro komatiite used in the present experiments. Visible phases include light gray spinifex tremolite (T) after cpx, medium gray olivine cores (O) mantled by cpx (X), devitrified glass (G), bright magnesiocromite (C), and bright magnetite veins (M). C: Backscattered image of sulfide accessory assemblage in Munro komatiite. Dark gray magnetite (M), medium gray chalcopyrite (Cp), and light gray pentlandite ± sphalerite (N). D: Backscattered image of Cu–Zn alloy in NAT1 run products.

Table 2
Chromite compositions.

	Munro	Stillwater	Fe-chromite ^a
<i>Mass %^b</i>			
Al ₂ O ₃	14.4	17.9	–
Cr ₂ O ₃	52.9	44.3	68
FeO	18.4	25.9	32
MgO	13.6	11.0	–
MnO	–	0.3	–
NiO	0.1	0.1	–
TiO ₂	–	0.5	–
Total	99.4	100.0	100
<i>Atomic % (normalized to 100%)</i>			
Al	17.9	22.3	–
Cr	44.3	37.0	66
Fe	16.3	22.8	34
Mg	21.5	17.4	–
Mn	–	0.3	–
Ni	0.1	0.1	–
Ti	–	0.2	–
<i>Selected compositional parameters</i>			
Cr/(Cr + Al)	0.62	0.71	1.0
Fe ⁺² /(Fe ⁺² + Mg)	0.31	0.20	1.0
Mg/Fe	0.74	0.42	–

^a Fe-chromite is the idealized endmember, Fe⁺²Cr₂O₄, used in Foustoukos and Seyfried (2004).

^b Analyses were performed by electron microprobe.

model composition for Fred's Flow, a layered flow in Munro Township (Kinzler and Grove, 1985). The glass was fused at 1450 °C from oxides in a gas mixing furnace at an f_{O_2} equal to the quartz–fayalite–magnetite buffer (QFM): an appropriate redox state for komatiitic magmas (Canil, 1997). Ni, Cu, Zn, Cr, and S were omitted from the glass in order to isolate any effect of the accessory assemblages in the NAT experiment. Chemical homogeneity in the glass on the scale of a few microns was confirmed via electron microprobe analyses.

To assess possible catalysis by magnesiocromite, natural chromitite from the Stillwater Complex was added to both NAT1 and SYN1 to

Table 3
Electron microprobe analyses of sulfide and alloy compositions.

	Pentlandite	Chalcopyrite	Sphalerite	Cu–Zn alloy
<i>Mass %</i>				
S	31.8	35.0	33.1	0.1
Cu	0.1	35.4	3.8	65.8
Fe	22.1	29.5	5.5	1.5
Ni	34.4	0.2	0.2	0.0
Zn	0.1	0.1	61.5	33.3
Co	9.7	0.1	0.1	0.0
Total	98.2	100.2	104.3	100.7
<i>Atomic % (normalized to 100%)</i>				
S	46.3	50.0	48.3	0.1
Cu	0.1	25.5	2.8	65.8
Fe	18.4	24.2	4.6	1.7
Ni	27.4	0.2	0.2	0.0
Zn	0.1	0.0	44.0	32.4
Co	7.7	0.1	0.1	0.0

create the chromitite-enriched bulk compositions NAT2 and SYN2 (Table 1). Mg/Fe and Cr₂O₃ were slightly lower in the Stillwater magnesiochromite than in the Munro magnesiochromites (Table 2), reflecting equilibration with a more mafic magma. The presence of MgO and Al₂O₃ distinguishes both magnesiochromites from the synthetic endmember Fe-chromite used in a previous methanogenesis experiment (Foustoukos and Seyfried, 2004). The modal abundance of magnesiochromite in the Stillwater chromitite was greater than 90%, with the remainder comprising accumulative olivine and minor pyroxene. The presence of minor olivine and pyroxene is assumed not to have influenced reaction rates because no silicate mineral has ever been found to catalyze hydrothermal CH₄.

All bulk silicate powders were plotted on a Jensen cation plot (Fig. 2) (Jensen, 1976). NAT1, NAT2, and SYN1 fall entirely within the ultramafic komatiite field, while SYN2 plots near the boundary between basaltic and ultramafic komatiites. All are less MgO-rich than the model mantle pyrolite (Green and Ringwood, 1963), and together they define a typical komatiite trend (Arndt and Nisbet, 1982). All samples were powdered in a tungsten carbide shatterbox. Particle size analyses were performed by a combination of mechanical sieves and SEM imaging. The average particle size of the komatiite and San Carlos olivine powders was 1–4 μm; the average size of the Stillwater chromitite particles was 4–6 μm.

The powders were loaded into the Au reactor of a flexible cell apparatus (Seyfried et al., 1987; McCollom and Seewald, 2001) with a formic acid–NaCl solution. Fluid–rock ratios are listed in Table 4. The solution was prepared from ultrapure water (18 MΩ), isotopically labeled formic acid (H¹³COOH), and NaCl at concentrations of 73–84 mmolal H¹³COOH (Table 1) and 0.5 molal NaCl. Labeled formic acid was used to distinguish between CH₄ formed by reduction of CO₂ present in the initial solution versus that formed from thermal cracking of organic contaminants (McCollom and Seewald, 2001). After annealing, the reactor was sealed with a Ti closure piece, loaded into a steel autoclave, and heated and pressurized to 300 °C and 350 bars. The experimental conditions and apparatus were equivalent to those used in a previous olivine serpentinization experiment (McCollom and Seewald, 2001), enabling direct comparison between studies.

At 300 °C, formic acid completely and rapidly decomposes to H₂ and CO₂ (Yu and Savage, 1998; McCollom and Seewald, 2003). Previous studies have already demonstrated that hydrothermal alteration of ultramafic materials by pure H₂O will generate fluids with high

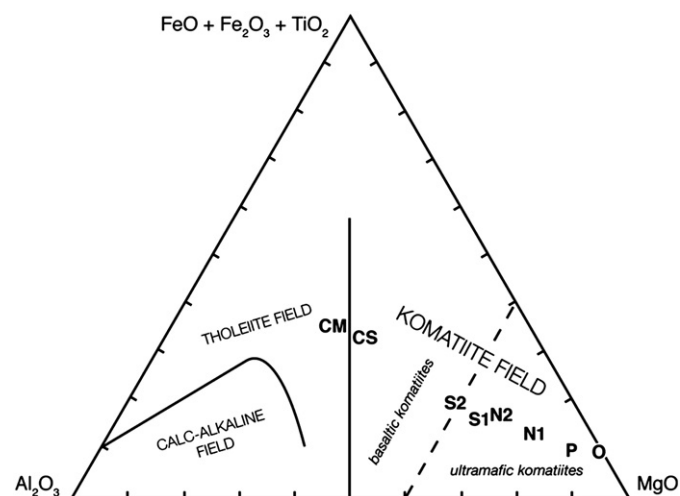


Fig. 2. Jensen cation plot (Jensen, 1976) of the starting compositions of experimental powders NAT1 (N1), NAT2 (N2), SYN1 (S1), and SYN2 (S2), and selected rock compositions. P=pyrolite, O=San Carlos olivine, CM=Munro magnesiochromite, CS=stillwater magnesiochromite. Solid lines delineate the boundaries between major volcanic rock series: calc-alkaline, tholeiites, and komatiites. The dashed line divides the komatiite field into basaltic and ultramafic domains.

Table 4

Mass of powders and fluids. The lower mass of material in SYN2 was due to a smaller reaction cell relative to that used for the other three experiments.

	NAT1	NAT2	SYN1	SYN2
Natural Munro komatiite	13.0	13.0	–	–
Synthetic glass	–	–	8.5	3.9
San Carlos olivine	–	–	2.9	1.3
Stillwater chromitite	–	3.0	–	1.2
Total solids	13.0	16.0	11.4	6.4
Fluid added (after initial bleed)	42.2	42.9	42.3	30.3
Initial fluid–rock ratio by mass	3.2	2.7	3.7	4.7

[H₂] via hydrolysis on month-long timescales (McCollom and Seewald, 2001; Yoshizaki et al., 2009). Therefore, the rapid introduction of H₂ at the beginning of the experiments had the practical advantage of substantially decreasing the time required to reach reducing conditions wherein in CH₄-rich fluids are stable.

Fluid samples were extracted at selected time intervals using a lockable gas syringe and subsequently injected into a gas chromatograph (GC). At room temperature, phosphoric acid was added to the fluid samples to convert any residual bicarbonate or carbonate ions to CO_{2(g)}. Thus, the reported CO₂ measurements are denoted as ΣCO₂, the sum of the concentrations of all carbonate species: CO₂, HCO₃[–], and CO₃^{2–}. Methane and hydrogen solubilities are vanishingly small at room temperature (Bonham, 1978; Seward and Franck, 1981); thus, the samples were not treated to optimize analysis of those species.

The values for [¹³CH₄] and [¹³CO₂] were calculated by combining GC concentration data with mass spectra analyzed using a gas chromatograph mass spectrometer (GC-MS). Relative concentrations of labeled and unlabeled methane were derived using the count ratios of CH₄⁺ to CH₃⁺ computed from averaged mass spectra of the unlabeled calibration gas (McCollom and Seewald, 2001). Isobaric interferences of OH⁺ and O₂⁺ from air were corrected by subtracting the background mass spectra averaged from both sides of the methane peak. An uncertainty of ±5% was assigned to the reported percentages of labeled CH₄ and CO₂ based on an empirical assessment of the error associated with selecting integration limits for the peak-averaged spectrum, which determined both the background interference and the average mass-to-charge ratios.

Equilibrium thermodynamic calculations were performed using the SUPCRT92 program (Johnson et al., 1992) with the slop98.dat database (geopig.asu.edu). The adopted standard state for minerals was unit activity of the pure phase at pressure and temperature. For aqueous species, the standard state was unit activity of a hypothetical 1 molal solution referenced to infinite dilution at pressure and temperature. For gaseous species, the standard state was unit fugacity of the pure gas at 1 bar and any temperature. Because the mole fraction of H₂O was greater than 0.99, water activity was approximated to be unity. The activity coefficients for CO_{2(aq)}, H_{2(aq)}, and CH_{4(aq)} were computed to be 0.23 using the CO_{2(aq)} formulation of Drummond (1981). Ionic strength was approximated to be equal to the NaCl molality.

3. Results

3.1. Solids

X-ray diffraction (XRD) analyses of the NAT1 products showed that calcite and serpentine grew, whereas olivine abundance decreased. No change in pyroxene or amphibole abundance was detected. The magnetite mode was approximately unchanged. The very fine grain size and tendency for disaggregated particles to spall off during polishing complicated microprobe analysis of accessory phases. Notwithstanding such difficulty, BSE imaging revealed a trace anhedral Cu–Zn alloy (Cu₆₈Zn₃₀Fe₂, alpha brass), typically less than 5 μm in diameter (Fig. 1D) and a likely desulfidation product of chalcopyrite and sphalerite. Only one Ni-bearing product was observed in a low-count probe analysis on a very small grain (<3 μm). The only elements detected during analysis of the

cryptic grain were Ni and S, but no Fe. Consistent with the decomposition of sulfides, a distinct hydrogen sulfide odor was detected upon opening the reaction cell.

Similar study of SYN1 revealed that olivine plus glass reacted to a fine-grained, indurated aggregate of serpentine, calcite, saponite, and fibrous xonotlite: $\text{Ca}_6\text{Si}_6\text{O}_{17}(\text{OH})_2$, a mineral found in rodingites (Esteban et al., 2003). There were no magnetic phases in the SYN1 post-run materials, indicating that magnetite was absent and that Fe was partitioned into serpentine and/or saponite. Except for the addition of chromite, the solid products for NAT2 and SYN2 were similar to NAT1 and SYN1.

3.2. Volatiles

Fluid analyses are listed in Table 5 and shown graphically in Figs. 3–6. In all four experiments, $[\text{H}_2]$ decreased during the first 24 h and then converged to a steady state: at 70–75 mmolal in NAT1, NAT2, and SYN1, and at ~55 mmolal in SYN2 (Fig. 3A). Values of $[\text{H}_2]$ were used in conjunction with the equilibrium:



to compute the experimental oxygen fugacities via

$$\log f_{\text{O}_2} = 2 \log a_{\text{H}_2} - \log K_{(2)} \quad (3)$$

The average experimental steady state $\log f_{\text{O}_2}$ value was -36.8. $\log f_{\text{O}_2}$ of QFM at the experimental conditions is approximately -35.6; thus the experimental redox conditions were 1.2 log units below QFM.

The total concentration of all labeled and unlabeled CO_2 , $[\Sigma\text{CO}_2]$, generally decreased over time in all experiments (Fig. 3B). Within 1 week, $[\Sigma\text{CO}_2]$ in SYN1 and SYN2 dropped by about 98% to steady

state values of about 1 mmolal. For NAT1 and NAT2, these values decreased by about 90% over the duration of the experiment, but the drop was much more gradual than in SYN1 and SYN2. In experiment NAT2, $[\Sigma\text{CO}_2]$ appeared to reach a steady state, while $[\Sigma\text{CO}_2]$ in NAT1 continued to decrease even between the final measurements. The decreasing slope of the NAT1 $[\Sigma\text{CO}_2]$ data with time suggests that the values were approaching a steady state concentration of about 5–6 mmolal. Comparing absolute concentrations between the experiments, the steady state $[\Sigma\text{CO}_2]$ values in NAT1 and NAT2 were roughly 4–5× higher than in the respective SYN experiments. In almost all experiments, $^{13}\text{CO}_2$ comprised ~70–95% of the total $[\Sigma\text{CO}_2]$ (Table 5).

The contrast in $[\Sigma\text{CO}_2]$ behavior between the NAT and SYN experiments may be attributed to calcite precipitation. The P–T conditions of both experiments were much closer to the original peak metamorphism experienced by the NAT komatiite than to the anhydrous melting conditions of the SYN glass. Thus, the energetic difference between the initial powder and the equilibrium phase assemblage was much greater in the SYN runs, inducing rapid dissolution of CaO from the highly reactive glass. Calcite crystallization within the first 24 h caused $[\Sigma\text{CO}_2]$ to drop precipitously to a steady state. In contrast, calcite precipitation in NAT1 was rate-limited by Ca dissolution from comparatively stable diopside and tremolite; thus, CO_2 did not decrease as rapidly.

The total CH_4 concentration of all labeled and unlabeled methane, $[\text{CH}_4]_{\text{tot}}$, increased steadily over time in all experiments (Fig. 4). Unlike $[\Sigma\text{CO}_2]$, $[\text{CH}_4]_{\text{tot}}$ did not appear to reach a steady state in any experiment. At 1500 h, $[\text{CH}_4]_{\text{tot}}$ values in NAT1 and NAT2 were roughly 7× greater than the respective SYN experiments, and roughly one third higher in the chromite-added experiments than in the respective chromite-free experiments. At 1500 h, $^{13}\text{CH}_4$ was 4× higher in NAT1 and NAT2 than in SYN1 and SYN2 (Fig. 5). The percentage of $^{13}\text{CH}_4$ ($\%^{13}\text{CH}_4$) rose steadily in each experiment, although faster in the chromite-free experiments (Table 5). At 1500 h, $\%^{13}\text{CH}_4$ in both the chromite-free

Table 5

Results: measured and computed experimental fluid compositions, 300 °C, 350 bars. Concentrations in mmolal. *Estimated analytical uncertainties are ±5% (McCullom and Seewald, 2001). †: uncertainties computed using standard error propagation formulas. Starting compositions of $[\text{H}_2]$ and $[\text{CO}_2]$ were assumed to be equal to the initial measured concentration of formic acid. Starting $\%^{13}\text{CO}_2$ was assumed to be 100%. Starting $[\text{CH}_4]_{\text{tot}}$, $\%^{13}\text{CH}_4$, and $^{13}\text{CH}_4$ were assumed to be zero.

Time (h)	$[\text{H}_2]^*$	$[\Sigma\text{CO}_2]^*$	$\%^{13}\text{CO}_2^*$	$^{13}\text{CO}_2^\dagger$	$[\text{CH}_4]_{\text{tot}}^*$	$\%^{13}\text{CH}_4^*$	$^{13}\text{CH}_4^\dagger$	$\%^{13}\text{CO}_{2\text{init}}$ converted to $^{13}\text{CH}_4^\dagger$
NAT1								
0	77	77	~100	77	~0	~0	~0	~0
22	72.9	39.6	–	–	0.12	–	–	–
166	71.2	12.7	–	–	0.15	–	–	–
532	71.5	9.9	89	8.8 ± 1.0	0.18	17	0.03 ± 0.00	0.04 ± 0.00
1056	71.8	7.0	–	–	0.21	–	–	–
1680	73.0	6.4	73	4.7 ± 0.4	0.26	34	0.09 ± 0.01	0.11 ± 0.01
NAT2								
0	79	79	~100	79	~0	~0	~0	~0
38	63.5	30.5	–	–	0.17	–	–	–
159	67.2	14.7	–	–	0.21	–	–	–
688	73.3	11.1	91	10.1 ± 0.7	0.29	13	0.04 ± 0.00	0.05 ± 0.00
1239	68.5	9.2	–	–	0.31	–	–	–
1552	70.0	9.2	73	6.7 ± 0.3	0.33	15	0.05 ± 0.00	0.06 ± 0.00
2680	74.1	9.3	94	8.7 ± 1.0	0.36	17	0.06 ± 0.01	0.08 ± 0.01
SYN1								
0	84	84	~100	84	~0	~0	~0	~0
22	59.2	32.5	–	–	0.00	–	–	–
187	77.4	1.3	–	–	0.01	–	–	–
377	74.3	1.0	87	0.9 ± 0.1	0.02	23	0.00 ± 0.00	0.00 ± 0.00
888	71.2	1.4	–	–	0.03	–	–	–
1512	74.1	1.6	52	0.9 ± 0.1	0.04	55	0.02 ± 0.00	0.02 ± 0.00
SYN2								
0	73	73	~100	73	~0	~0	~0	~0
19	62.8	28.0	–	–	0.02	–	–	–
137	52.5	1.0	–	–	0.02	–	–	–
667	56.7	1.1	85	0.9 ± 0.3	0.03	21	0.01 ± 0.00	0.01 ± 0.00
1215	54.2	1.4	–	–	0.04	–	–	–
1526	55.4	1.7	93	1.6 ± 0.2	0.05	27	0.01 ± 0.00	0.02 ± 0.00

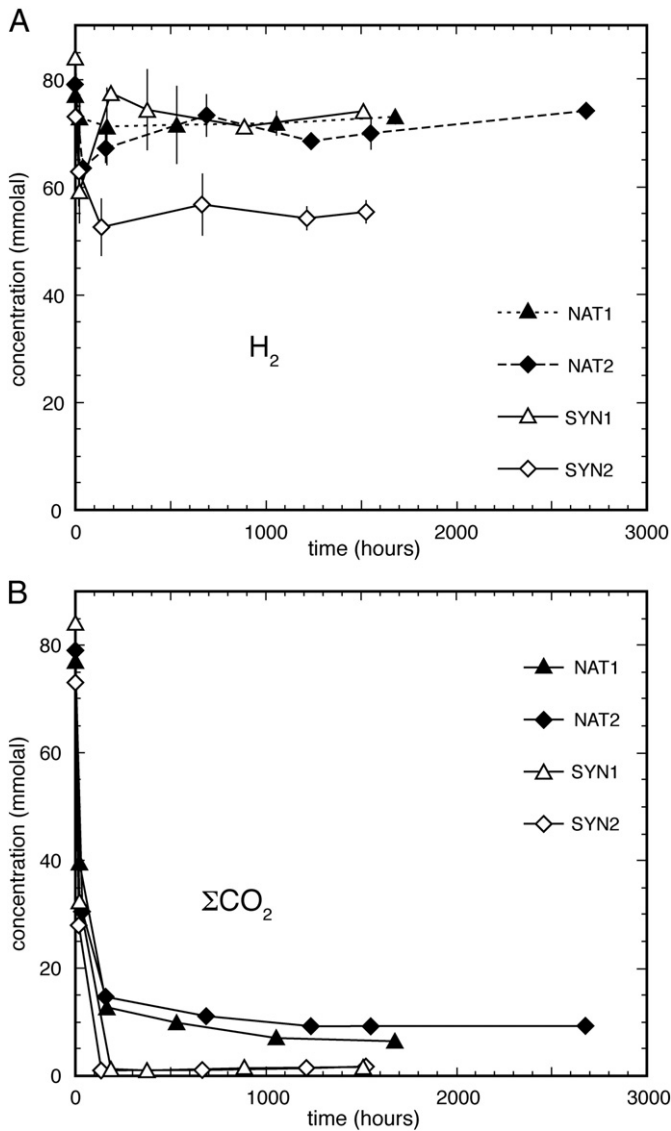


Fig. 3. $[H_2]$ (A) and $[\Sigma CO_2]$ (B) versus time. Estimated analytical uncertainties are $\pm 5\%$. Error bars are shown where larger than the symbol size.

experiments was about twice as high as in the respective chromite-added experiments. With the exception of the final measurement of SYN1, $\%^{13}CH_4$ was always less than 35% of the total methane, a significantly lower proportion of labeled carbon than seen in the CO_2 measurements. No ^{13}CO nor labeled hydrocarbon of a higher order than methane was detected.

The observation that $[\Sigma CO_2]$ and $[CH_4]_{tot}$ in every experiment contained both labeled and unlabeled carbon highlights the importance of using labeled formic acid to distinguish between carbon sources (McCollom and Seewald, 2001). The unlabeled methane could have been derived from several possible sources, including (1) reduction of unlabeled CO_2 , (2) thermal decomposition of natural organics present within the minerals (Tingle et al., 1990), and (3) thermal decomposition of contaminants introduced during sample handling and storage. Volatilization of carbonaceous material during fusion of the synthetic glass at 1450 °C significantly reduced the level of contamination in the SYN experiments relative to the NAT experiments. For example, the concentration of unlabeled CH_4 in NAT2 at 1552 h was 0.28 mmolal, whereas the concentration of unlabeled CH_4 in SYN2 at 1526 h was 0.04 mmolal.

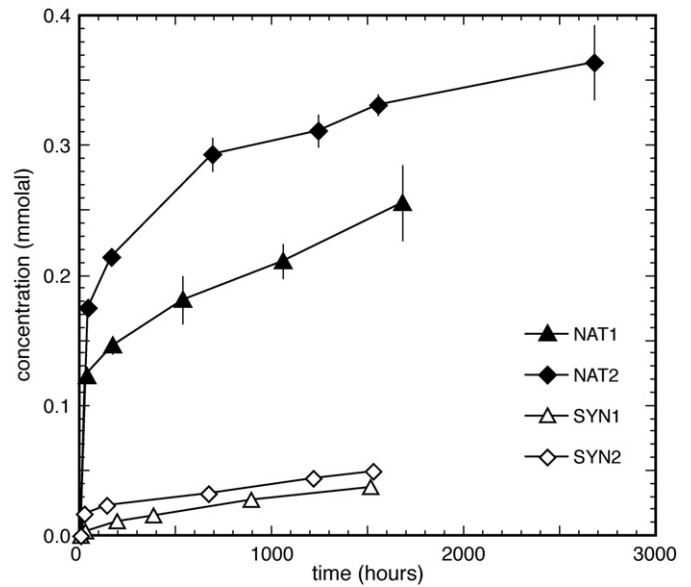


Fig. 4. $[CH_4]_{tot}$ versus time. Estimated analytical uncertainties are $\pm 5\%$. Error bars are shown where larger than the symbol size.

In all experiments, the value of $[CH_4]_{tot}$ was always lower than the concentration required to satisfy equilibrium in Reaction (1). To illustrate, the $[CH_4]/[CO_2]$ ratios required for equilibrium with the measured $[H_2]$ values were computed using the equilibrium constant for Reaction (1). The resulting $[CH_4]/[CO_2]$ values were on the order of 10^4 for all experiments, or six orders of magnitude higher than the measured $[CH_4]_{tot}/[\Sigma CO_2]$ ratios, indicating that $[CH_4]_{tot}$ values were well below equilibrium.

4. Discussion

4.1. Comparison of CH_4 yields in natural and synthetic komatiite experiments

The fractional conversion of $^{13}CO_2$ to $^{13}CH_4$ with time is shown in Fig. 6. The data were fit to $F = At^B$, where F is fractional conversion in percent and t is time in hours. Fit parameters A and B are given in

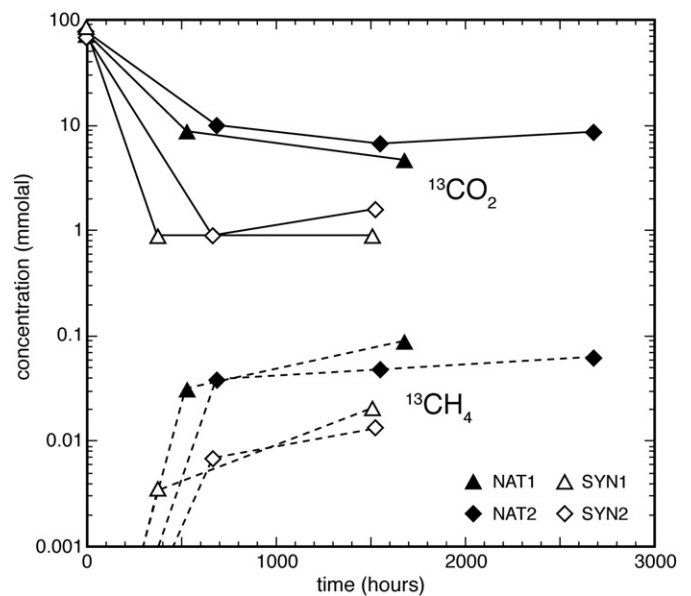


Fig. 5. $[^{13}CO_2]$ (solid lines) and $[^{13}CH_4]$ (dashed lines) in experimental fluids versus time. Error bars are propagated uncertainties and are shown where larger than the symbol size.

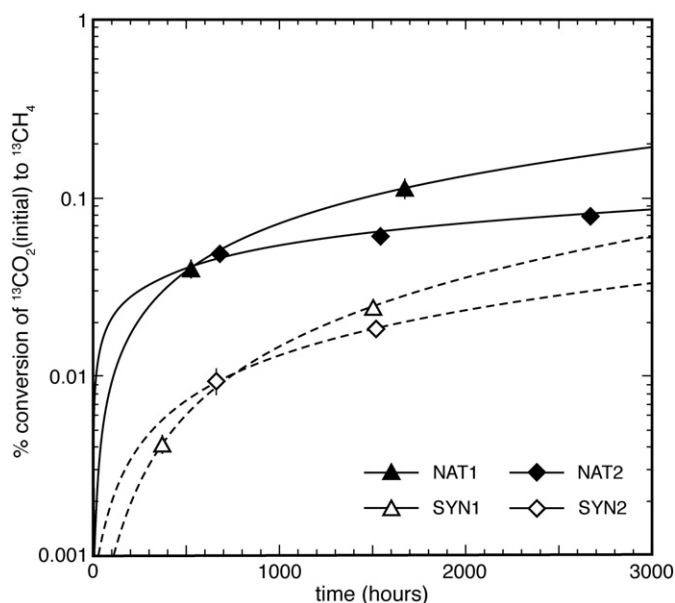


Fig. 6. Fractional conversion of $[^{13}\text{CO}_2]_{\text{initial}}$ to $[^{13}\text{CH}_4]$, in percent, versus time, 300 °C, 350 bars. The values for $[^{13}\text{CO}_2]_{\text{initial}}$ were set to the initial formic acid concentrations (Table 5). Lines are power law fits to the data, $F = At^B$, where F is percent conversion and t is time in hours. Fit parameters are given in Table 6. Error bars represent propagated uncertainties and are shown where larger than the symbol size.

Table 6. The conversion of $^{13}\text{CO}_2$ to $^{13}\text{CH}_4$ in the presence of the natural komatiite was greater than in the presence of the synthetic komatiite. For example, at 1500–1600 h, the fractional conversion in the NAT1 experiment was roughly four times higher than in SYN1.

Homogeneous effects cannot easily explain the difference in $^{13}\text{CH}_4$ yields. Reaction (1) suggests a rate dependence of methanogenesis on $[\text{H}_2]$. However, steady state $[\text{H}_2]$ values were nearly identical in NAT1 and SYN1, and differed by only 25% between NAT2 and SYN2 (Table 5). Thus, $[^{13}\text{CH}_4]$ did not clearly correlate with $[\text{H}_2]$. Reaction (1) also suggests a rate dependence of methanogenesis on $[\text{CO}_2]$. Steady state $[\Sigma\text{CO}_2]$ values in the NAT experiments were 4–5 times higher than in the SYN experiments (Table 5), suggesting that the observed difference in $^{13}\text{CH}_4$ yield directly correlated with $[\Sigma\text{CO}_2]$. However, such an interpretation is inconsistent with other observations. For example, at about 1600 h, the steady state $[\Sigma\text{CO}_2]$ values in NAT2 were ~50% higher than NAT1, despite the observation that $[^{13}\text{CH}_4]$ in NAT1 was twice as high as in NAT2. Furthermore, the $[\Sigma\text{CO}_2]$ values in a previous olivine serpentinization experiment at otherwise identical conditions (McCullom and Seewald, 2001) were higher (~10 mmolal) than the steady state values in the NAT1 experiments (~5–6 mmolal). However, $[^{13}\text{CH}_4]$ in the olivine experiment was similar to that measured in the SYN experiments (Fig. 7), suggesting that $[\Sigma\text{CO}_2]$ does not reproducibly correlate with $[^{13}\text{CH}_4]$.

We propose instead that heterogeneous catalysis can explain the difference in CH_4 yields between the NAT, SYN, and previous

Table 6

Coefficients for power law fits ($F = At^B$) to data for fractional conversion of $^{13}\text{CO}_2$ to $^{13}\text{CH}_4$ from this study and previous work (Figs. 6 and 7). F is fractional conversion in percent and t is time in hours. Mt = magnetite; chr = chromite.

Experiment	Data source	A	B
NAT1	Table 5	1.4E–04	0.9
NAT2	Table 5	2.7E–03	0.4
SYN1	Table 5	1.8E–06	1.3
SYN2	Table 5	3.6E–05	0.9
FS mt + chr	Foustoukos and Seyfried (2004)	5.0E–05	1.3
FS mt	Foustoukos and Seyfried (2004)	8.5E–07	1.7
Olivine	McCullom and Seewald (2001)	3.0E–06	1.2

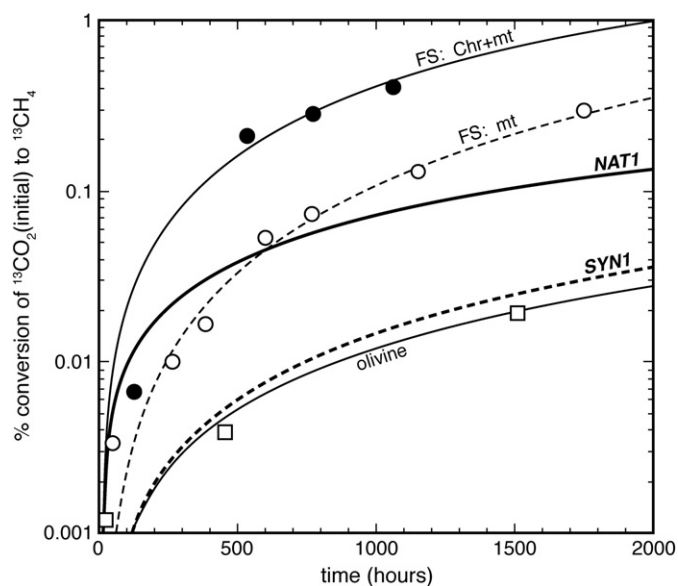


Fig. 7. Fractional conversion of $[^{13}\text{CO}_2]_{\text{initial}}$ to $[^{13}\text{CH}_4]$ over time for NAT1 and SYN1 at 300 °C and 350 bars; chromite + magnetite (chr + mt, black circles) and magnetite-only (mt, white circles) at 390 °C and 400 bars (Foustoukos and Seyfried, 2004); and olivine (white squares) at 300 °C and 350 bars (McCullom and Seewald, 2001). The values for $[^{13}\text{CO}_2]_{\text{initial}}$ were set to the input formic acid concentrations. Lines are power law fits to the data, $F = At^B$. Fit parameters are given in Table 6. Error bars represent propagated uncertainties and are smaller than the symbol size.

olivine serpentinization experiments. Several recent papers have demonstrated the importance of FTT catalysis during aqueous methanogenesis (see Section 1), and potential catalysts were present in the natural komatiites but not in the synthetic experiments or previous olivine experiments. In the next section, each candidate mineral is evaluated for its potential catalytic contribution to the observed rates of methanogenesis.

4.2. Inventory of potential FTT catalysts

4.2.1. Magnesiochromite

Magnesiochromite was a possible FTT catalyst in the NAT1 experiments because it was present in NAT1 but absent in SYN1. To illustrate this potential, the chromite–magnetite and magnetite-only experiments of Foustoukos and Seyfried (2004) were fit to power law functions (Table 6) and plotted with the NAT1 and SYN1 trends Fig. 7. These experiments were performed at higher temperature (390 °C) than the current experiments, which likely explains the observation that the absolute conversion rates were roughly an order of magnitude higher than the NAT1 and SYN1 experiments. More relevant to the interpretation of the current experiments is the relative conversion rates: the chromite–magnetite experiment generated $^{13}\text{CH}_4$ at a faster rate than the magnetite-only experiment. The difference in methane conversion between the experiments was ~4× at ~1100 h: roughly the same difference as between NAT1 and SYN1. By extension, catalysis by magnesiochromite may have increased the rate of methanogenesis in the NAT experiments relative to the SYN experiments.

This hypothesis was tested by performing the magnesiochromite-enriched experiments NAT2 and SYN2. However, the conversion rates measured in these experiments were lower, not higher, than in the respective NAT1 and SYN1 experiments (Fig. 6). A possible explanation for this observation is that increasing MgO and/or Al_2O_3 activity may reduce the catalytic effect of endmember Fe-chromite, implying that the range of natural chromite compositions favorable for methanogenesis is restricted.

4.2.2. Magnetite

Magnetite, another spinel group mineral common in serpentinites, has been proposed to be an FTT catalyst during aqueous methanogenesis (Berndt et al., 1996). It was present in NAT1 but absent in SYN1, implying that it may have catalyzed CH₄ formation. However, no methanogenesis was observed in previous hydrothermal formic decomposition experiments in the presence of magnetite plus hematite at 250 °C (McCullom and Seewald, 2003) and magnetite only at 400 °C (Horita and Berndt, 1999), suggesting that magnetite is not a suitable aqueous catalyst at hydrothermal conditions. Furthermore, magnetite formed in the McCollom and Seewald olivine serpentinization experiment (2001) performed at identical pressure, temperature, and starting [H¹³COOH] (Fig. 7), yet the rate of labeled methane production was similar to the magnetite-free SYN experiments. Therefore, magnetite in NAT1 was not likely catalytic.

4.2.3. Cu–Zn alloy

Ni–Fe alloy has been shown to enhance CH₄ yields in hydrothermal experiments at similar conditions to the present study (Horita and Berndt, 1999; McCollom and Seewald, 2003; Lazar et al., submitted for publication). This implies that the Cu–Zn alloy observed in the NAT1 post-run products may have been catalytic with respect to CH₄. Whether Cu–Zn alloy catalyzes methane has not been directly addressed. Cody et al. (2004) pointed out, however, that Cu does not readily bond with C, and thus is a poor catalyst for organic reactions. This behavior was observed the Cody et al. hydrothermal experiments, in which Cu and Zn sulfides were the least catalytic among a suite of transition metal sulfides with respect to the formation of decanoic acid (CH₃(CH₂)₈COOH) at 250 °C.

4.2.4. Sulfides

The remaining possible transition metal catalysts in the experiments were sulfides. The identity of the cryptic nickel sulfide phase in the NAT1 products was deduced using the S-poor, H₂-rich portion of an *a*H₂S–*a*H₂ phase diagram of serpentinite accessory minerals in the system Ni–Fe–O–S at 300 °C and 500 bars (Fig. 8) (Klein and Bach, 2009). The bold

gray line denotes the average steady state *a*H₂ value in NAT1. The upper limit for *a*H₂S in NAT1 may be inferred from the presence of the Cu–Zn alloy and the intersection of the *a*H₂ value with the univariant line defined by the equilibrium:



The stability of this equilibrium is supported by a report of a Cu-alloy + chalcocite alteration assemblage in a natural komatiite (Hoatson et al., 2005). To estimate *a*H₂S, ideal mixing in the alloy was assumed, where *a*Cu_{alloy} = X_{Cu} ~ 0.7. Using the log K for Reaction (4), the y- intercept at 500 bars was computed to be log *a*H₂S = –3.43. At 350 bars, the y- intercept was –3.44, justifying the implicit assumption that the 150 bar difference between the experimental conditions and the conditions of the adopted diagram has a small impact on the relevant log K values.

Intersection of the alloy–chalcocite desulfidation curve with the *a*H₂ value leads to an upper constraint of log *a*H₂S ~ –5.2. This value is below the minimum *a*H₂S value of pentlandite stability, consistent with the fact that the initial experimental fluid was S-free. In other words, the sulfur activity of the experimental system was lower than the original conditions of pentlandite saturation, leading to the destabilization of pentlandite with respect to a new Ni phase containing less sulfur.

Over the inferred range of permissible log *a*H₂S values for NAT1, only two Ni-bearing phases are possible: awaruite (Ni₃Fe) and heazlewoodite (Ni₃S₂). Since microprobe analyses indicated the coexistence of Ni and S, the cryptic nickel sulfide was likely heazlewoodite. This requires that the lower *a*H₂S limit must have been the awaruite–heazlewoodite phase transition at log *a*H₂S ~ –7. Consistent with these constraints, pentlandite reacted with the fluid to form heazlewoodite and magnetite via:

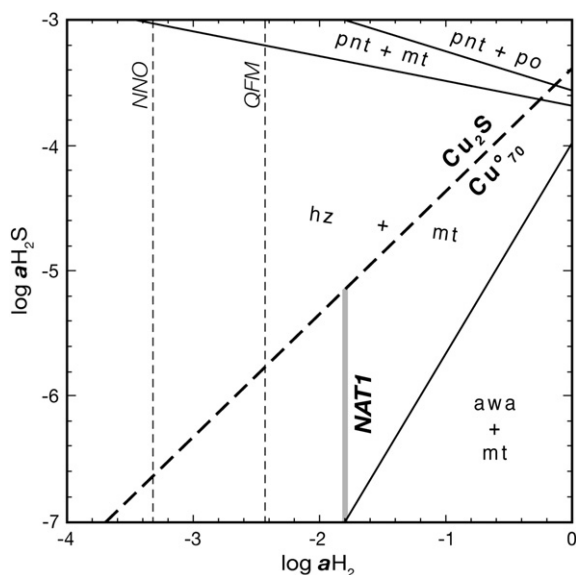


Fig. 8. Activity-activity diagram in the system Ni–Fe–S–O–H, 300 °C, 500 bars, fluid saturated. Phase boundaries (thin solid lines) are adapted from Klein and Bach (2009). Cu₇₀–Cu₂S equilibrium is computed from Reaction (4), assuming ideal solution. Awa = awaruite (Ni₃Fe); Pnt = pentlandite (Ni,Fe)₉S₈; hz = heazlewoodite (Ni₃S₂); mt = magnetite (Fe₃O₄); po = pyrrhotite (Fe_{1–x}S). The gray line represents the inferred range of possible experimental conditions in NAT1. For reference, vertical dashed lines represent the *a*H₂ value buffered by the buffer assemblages, nickel–nickel oxide (NNO) and quartz–fayalite–magnetite (QFM).

With the identification of heazlewoodite, the complete inventory of observed sulfide minerals in the experimental reactants and products is: chalcopyrite, sphalerite, pentlandite, and heazlewoodite, all of which have been previously studied as organic catalysts. Cody et al. (2004) reported that heazlewoodite was an order of magnitude more effective than chalcopyrite or sphalerite in promoting the formation of decanoic acid. Catalysis by pentlandite occurred at a rate intermediate between heazlewoodite and the chalcopyrite and sphalerite. Cody et al. concluded that Ni minerals were generally the most catalytic, relative to the other sulfides in their study. Consistent with this conclusion, Fu et al. (2008) reported the synthesis of labeled methane and surface-bound hydrocarbons during hydrothermal synthesis of pentlandite, and reported the presence of heazlewoodite in the run products. By extension, heazlewoodite and/or pentlandite may have been catalytic in NAT1 and NAT2. The relative importance of heazlewoodite and pentlandite is uncertain, but two lines of indirect evidence suggest a greater role for heazlewoodite. First, the conclusion of Cody et al. that Ni enhances organic reaction yields suggests that the more Ni-rich heazlewoodite may be more catalytic than pentlandite. Second, because the experimental fluids were initially S-free, pentlandite was unstable and may have rapidly converted to heazlewoodite. Thus, heazlewoodite was likely present for a longer duration of the experiment than pentlandite.

4.3. CH₄ yields in the Hadean and Archean

The interpretation that Ni-sulfides catalyzed methane in the NAT experiments has important implications for methanogenesis on the early Earth. Not only does komatiite serpentinization lead to the requisite reducing conditions for CH₄ production, but in addition komatiites possess

notably high concentrations of Ni and S (Arndt et al., 2008). Ni concentrations are elevated in komatiites due to the compatibility of Ni in source minerals relative to silicate melt (Sato, 1977). Since the concentration of such compatible elements in a melt increases with the degree of partial melting, komatiites contain more Ni than tholeiitic basalts. Sulfur, on the other hand, is highly incompatible with respect to residual mantle minerals during melting (Lorand, 1991). This leads to sulfide saturation at the mantle source in the low degree partial melts that generate tholeiitic basalt, and the consequent immobilization of S in the residual mantle (Keays, 1995). In contrast, the higher degree partial melts attending komatiite formation result in lower S concentrations at the source. Sulfide-saturation is delayed until cooling occurs after eruption or during near-surface crystallization, aided by the inverse relationship of pressure with sulfide solubility in silicate melts (Mavrogenes and O'Neill, 1999). Since Ni is chalcophile (Maclean and Shimazaki, 1976), the relatively high concentrations of Ni and S in the near-surface melt result in a high modal abundance of magmatic Ni-sulfides that are potentially accessible to infiltrating seawater and CH₄-generating hydrothermal metamorphism.

Field evidence supports high Ni and S in the early Precambrian, when komatiitic magmatism produced a global distribution of economically important Ni–Cu–PGE sulfide deposits (Arndt et al., 2008). Moreover, many komatiites that are not associated with economic base-metal ore deposits contain at least trace amounts of Ni-sulfides. Independent evidence supports a high volcanic flux of nickel to the Archean crust: Ni/Fe ratios in banded iron formations (BIFs) were high throughout most of the eon, but decrease sharply at 2.7 Ga, mirroring the decline of komatiites in the rock record (Konhauser et al., 2009). No BIFs are preserved before 3.8 Ga, but the high Ni/Fe trend would likely have been present in the Hadean, since mantle potential temperatures would have been even higher than in the Archean.

Despite the favorability for the precipitation of pentlandite and/or heazlewoodite during the crystallization of high degree partial melts, field evidence suggests that nickel sulfides are not restricted to ultramafic compositions. Although the largest sulfide deposits tend to be associated with peridotitic lithologies, magmatic pentlandite has been documented in basaltic and pyroxenitic komatiites at Munro Township (Stone et al., 1996), and even in high-Mg basalts within basaltic layered intrusions (Godel and Barnes, 2008). Since the current experiments suggest that a few tenths of a percent by volume of heazlewoodite and/or pentlandite can accelerate methanogenesis, the existence of even trace Ni-sulfides in basaltic and pyroxenitic komatiites may significantly expand the volumetric fraction of the early Precambrian oceanic crust containing suitable CH₄ catalysts.

Komatiitic volcanism also favored the formation of other catalysts in addition to Ni-sulfides. Although the present results suggest that magnesiocromite is catalytically inactive with respect to methanogenesis, they do not contradict the conclusion of Foustoukos and Seyfried (2004) that endmember Fe-chromite enhances methane yields at hydrothermal conditions. Of relevance to the early Precambrian, Fe-chromite with Cr/(Cr + Al + Fe³⁺) > 0.9 is typically associated with komatiite magmatism (Barnes and Roeder, 2001). Massive sulfide deposits in particular are known to host Fe-chromites with Cr/(Cr + Al + Fe³⁺) ≈ 1.0. Thus, the previous demonstration that endmember Fe-chromite catalyzes methane implies that this accessory mineral may have been an important catalyst on the early Earth, and would have increased yields beyond that produced by Ni-sulfides alone.

4.4. A simple model

Owing to differences in bulk composition, mineralogy, and crustal production rates, hydrothermal alteration of a komatiite-bearing oceanic crust on the early Earth was likely a more productive source for abiotic methane than serpentinization of the modern crust. To assess whether CH₄ from serpentinization of a komatiitic seafloor could have sustained

a nonglacial early Earth, Archean methane production rates were estimated by adapting the input parameters of a previously published calculation of methane flux from the modern seafloor (Emmanuel and Ague, 2007):

$$R_{CH_4} = V' Y_m C P_{L-M} \left(\frac{P_{Nz} M_{CH_4}}{M_{Nz}} \right) \quad (5)$$

where R_{CH_4} is the annual global CH₄ production rate (g/yr); V' is the volume fraction of serpentine in the ocean crust; Y_m is the yield of CH₄ from Reaction (1) calculated as $[CH_4]/([CH_4] + 0.25[H_2])$; C is the volumetric oceanic crustal production rate (m³/yr); P_{L-M} is the stoichiometric ratio of serpentine to methane during harzburgite serpentinization (Evans, 2008); ρ is density of serpentine (g/m³); and M is the molecular weight of methane and serpentine (g/mol). The variables C , Y_m , and V' are partly dependent on Earth's heat flow. For example, higher heat flow implies faster crustal production, C (Bickle, 1986). High heat flow also leads to high degree partial melts, which are more likely to be ultramafic (high V') and to contain catalysts (high Y_m) such as Ni-sulfides. Since heat flow has steadily decreased over Earth's history, it follows that the values for C , Y_m , and V' were higher in the early Precambrian than today.

Using fluid compositions from the extant seafloor serpentinite springs Rainbow and Logatchev, Emmanuel and Ague estimated the modern value of Y_m to be ~0.5. The current experiments suggest that Y_m in the Archean was higher than today because magmatic Ni-sulfides (and Fe-chromites) were more abundant in the early Precambrian than today. Although the modal abundance of sulfides was less than 1% in the Munro sample, the presence of massive sulfide deposits in Archean komatiite sequences indicates that Ni-sulfides were commonly more abundant than the 0.2–0.3 modal percent seen in NAT1. An accurate assessment of the highly variable catalyst abundance in the Precambrian crust is beyond the scope of this paper, and catalytic activity is also dependent on several other variables such as specific surface area, source rock porosity, temperature, and pressure. Nevertheless, to first order, Ni-sulfides were more abundant in the Precambrian than today; therefore, the present experimental results justify the assumption that Y_m was greater on the early Earth. To reflect this, and the uncertainty in catalyst abundance, two values of Y_m were selected: 0.5 and 1.0. The value of 0.5 reflects the modern yield from Rainbow. The value of 1.0 represents the maximum yield, permitting an exploration of the full range of parameter space.

Values for V' are also difficult to constrain and are highly variable in the Archean rock record. No unequivocal Archean ophiolite has been discovered, so V' was estimated from the volumetric fraction of ultramafic units in komatiitic sequences within greenstone belts. Such deposits are not believed to represent true oceanic crust (Bickle et al., 1994), yet they represent the best available field constraints on komatiite abundance in Archean volcanic sequences. Analyses of seven published sections of 3.2–3.5 Ga deposits in South Africa and 2.7 Ga deposits in Australia (Arndt and Nisbet, 1982) showed that 50–100% of the volume of greenstone volcanics comprised lithologies within the komatiite magma series, with the remainder composed of tholeiitic basalts. Ultramafic komatiites comprised 0–40% of the total komatiite volume (Arndt et al., 2008). However, other ultramafic units such as olivine cumulates can occur in the nominally mafic portions of komatiitic sequences. Two values for V' were selected: 0.5 and 1.0. The value of 0.5 represents a hypothetical crust containing 40% ultramafic komatiites and 10% other ultramafic units. The value of 1.0 represents a hypothetical crust that is completely ultramafic, permitting an exploration of the full range of parameter space.

Values of R_{CH_4} were adapted from a recent updated late Archean greenhouse model for a CH₄–CO₂ atmosphere with an assumed solar luminosity 20% lower than today (Haqq-Misra et al., 2008). In the model, R_{CH_4} values correspond to the methane flux required to sustain a given average global surface temperature as a function of partial pressure of CO₂ (pCO_2). The model was updated from a previous version

(Pavlov et al., 2000) with revised absorption coefficients that suggest the influence of methane on early Earth greenhouse warming was more limited than previously thought. That is, at constant $p\text{CO}_2$, increasing the partial pressure of methane ($p\text{CH}_4$) causes average global temperature to increase until a critical $p\text{CH}_4$ value above which a cooling hydrocarbon haze begins to form.

Using the R_{CH_4} values extracted from the Haqq-Misra et al. model, along with the estimates for V' and Y_m , Eq. (5) was solved for C . In other words, we computed the crustal production rate required to sustain a given global surface temperature as a function of $p\text{CO}_2$ and the selected petrologic model parameters in Eq. (5). The values for C and $p\text{CO}_2$ were normalized to present day values (C/C^{modern} and $p\text{CO}_2/p\text{CO}_2^{\text{modern}}$) (Fig. 9). Independent of the selected values of V' and Y_m , $p\text{CO}_2$ is required to be 65–75 times that of today, illustrating a significant role for CO_2 in regulating paleotemperature. For the cases $Y_m=1.0$ and $V'=0.5$ or $Y_m=0.5$ and $V'=1.0$, a solution to the Faint Young Sun problem requires a crustal production rate of at least ~25 times that of today (Fig. 9A). However, the most generous estimate for Archean spreading rates is only six times that of today (Bickle, 1978). Even in the case of maximum yield and ultramafic abundance, $Y_m=1.0$ and $V'=1.0$ (Fig. 9B), this crustal production rate would not have been sufficient to warm the early Earth to a nonglaciated temperature. Moreover, recent modeling has suggested that the Archean crustal production rate may have even been lower than today (Korenaga, 2003). An alternative parameter set may be derived from an often cited geodynamic model for Archean oceanic crust formation, which features a 20 km basaltic crust containing <15% ultramafic komatiite (Sleep and Windley, 1982). However, applying these parameters to Eq. (5) does not appreciably change the calculated methane flux because increased crustal thickness is largely offset by a comparable relative decrease in V' .

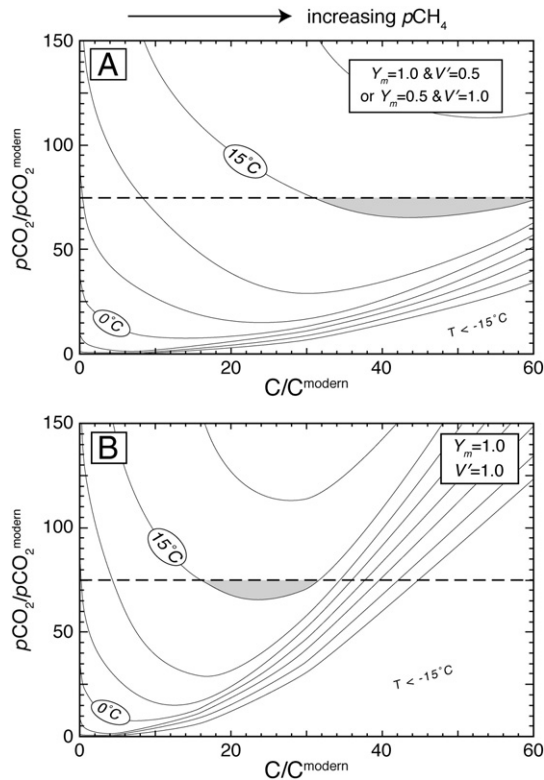


Fig. 9. Relationship of crustal production rate, C , and the partial pressure of CO_2 , $p\text{CO}_2$, to average global temperature, as adapted from an atmospheric model of an Archean greenhouse effect (Haqq-Misra et al., 2008) and a geodynamic expression from Emmanuel and Ague (2007). C and $p\text{CO}_2$ are normalized to modern values. Horizontal dashed line is the upper limit for Archean CO_2 based on paleosol constraints (Rye et al., 1995). Gray shaded regions are the permissible range of conditions for which the Faint Young Sun problem is resolved by serpentinization of a komatiitic seafloor, i.e., average global surface temperature is above 15°C . Solid lines are isotherms at 5°C intervals. Isotherms below -15°C are not shown.

The results of the above modeling suggest that serpentinization of a komatiitic oceanic crust cannot alone solve the Faint Young Sun problem. However, differences in C may still have exerted an important control on global temperature. For example, Fig. 9 implies that a crustal production rate $6\times$ higher than the modern rate at $p\text{CO}_2/p\text{CO}_2^{\text{modern}}=25$ would generate five degrees of warming: enough to affect global sea level. Our calculations are likely an underestimation of the total global abiotic flux in the early Precambrian due to the exclusion of a variety of additional potential sources, including metamorphism of plume-dominated greenstone volcanic systems (Arndt et al., 1997), serpentinization of the forearc mantle (Lazar et al., submitted for publication), diffuse mantle outgassing (Ingebritsen and Manning, 2002), continental hydrothermal systems (Fiebig et al., 2007), impacts (Kress and McKay, 2004), basalt alteration (Lyons et al., 2005), methanogenesis in crystalline basements (Sherwood Lollar et al., 2002), and serpentinization of oceanic mantle lithosphere (Schmidt and Poli, 1998; Li and Lee, 2006).

5. Conclusions

The current experiments suggest that Ni-sulfides may be important catalysts for hydrothermal abiotic methanogenesis. The failure of magnesiochromite to catalyze methane in the study suggests that the ability of chromite to enhance methanogenesis is limited to endmember Fe-chromite compositions. Due to the combination of a higher modal abundance of suitable catalysts, faster crustal production rates, and a greater volumetric proportion of ultramafic lithologies, the CH_4 flux from serpentinization of an Archean or Hadean oceanic crust was likely higher than that from metamorphism of the modern predominantly tholeiitic seafloor. By coupling a simple model for methane flux via seafloor serpentinization (Emmanuel and Ague, 2007) with an atmospheric model of an Archean greenhouse effect (Haqq-Misra et al., 2008), it was concluded that alteration of a komatiitic seafloor was insufficient to sustain a non-glacial Earth; i.e., it cannot solve the Faint Young Sun paradox. This does not rule out the possibilities that alteration of a komatiitic seafloor could have exerted a minor influence on climate or that the total geological flux of methane from all possible abiotic sources could have maintained a nonglaciated Earth.

Acknowledgments

We thank Mike Baker at Caltech for assistance with the gas mixing furnace, Jon Harrington for petrographic assistance, and Saeed Khan at UCLA for assistance with X-ray analyses. We thank N. Arndt, R. Hazen, associate editor J. Fein, and an anonymous reviewer for helpful comments that improved the manuscript. Ternary plotting was performed using the DPlot freeware, programmed by Cédric John and available for download at www.crog.org/cedric/dplot. This work was supported by grants from the NASA Astrobiology Institute (UCLA), the NASA Exobiology Program, the University of California Lab Research Program, and the Sloan Foundation.

References

- Arndt, N.T., Nisbet, E.G., 1982. Komatiites. Allen & Unwin, Oxford.
- Arndt, N.T., Naldrett, A.J., Pyke, D.R., 1977. Komatiitic and iron-rich tholeiitic lavas of Munro Township, Northeast Ontario. *Journal Of Petrology* 18, 319–369.
- Arndt, N.T., Albarede, F., Nisbet, E.G., 1997. Mafic and ultramafic magmatism. In: De Wit, M.J., Ashwal, L.D. (Eds.), *Greenstone Belts*. Clarendon Press, Oxford, p. 809.
- Arndt, N.T., Leshar, C.M., Barnes, S.J., 2008. Komatiite. Cambridge University Press.
- Barnes, S.J., Roeder, P.L., 2001. The range of spinel compositions in terrestrial mafic and ultramafic rocks. *Journal Of Petrology* 42, 2279–2302.
- Berndt, M.E., Allen, D.E., Seyfried, W.E., 1996. Reduction of CO_2 during serpentinization of olivine at 300°C and 500 bar. *Geology* 24, 351–354.
- Bickle, M.J., 1978. Heat loss from Earth — constraint on Archean tectonics from relation between geothermal gradients and rate of plate production. *Earth And Planetary Science Letters* 40, 301–315.
- Bickle, M.J., 1986. Implications of melting for stabilization of the lithosphere and heat-loss in the Archean. *Earth And Planetary Science Letters* 80, 314–324.
- Bickle, M.J., Nisbet, E.G., Martin, A., 1994. Archean greenstone belts are not oceanic-crust. *Journal of Geology* 102, 121–138.

- Bonham, L.C., 1978. Solubility of methane in water at elevated-temperatures and pressures. *Aapg Bulletin — American Association Of Petroleum Geologists* 62, 2478–2481.
- Canil, D., 1997. Vanadium partitioning and the oxidation state of Archaean komatiite magmas. *Nature* 389, 842–845.
- Carignan, J., Machado, N., Gariépy, C., 1995. U–Pb isotopic geochemistry of komatiites and pyroxenes from the Southern Abitibi greenstone-belt, Canada. *Chemical Geology* 126, 17–27.
- Carmichael, I.S.E., Turner, F.J., Verhoogen, J., 1974. *Igneous Petrology*. McGraw-Hill, (739 pp.).
- Charlou, J.L., Fouquet, Y., Donval, J.P., Auzenne, J.M., Jean-Baptiste, P., Stievenard, M., Michel, S., 1996. Mineral and gas chemistry of hydrothermal fluids on an ultrafast spreading ridge: East Pacific Rise, 17° to 19°S (Naudur cruise, 1993) phase separation processes controlled by volcanic and tectonic activity. *Journal of Geophysical Research* 101, 15899–15919.
- Charlou, J.L., Fouquet, Y., Bougault, H., Donval, J.P., Etoubleau, J., Jean-Baptiste, P., Dapigny, A., Appriou, P., Rona, P.A., 1998. Intense CH₄ plumes generated by serpentinization of ultramafic rocks at the intersection of the 15 degrees 20' N fracture zone and the Mid-Atlantic Ridge. *Geochimica et Cosmochimica Acta* 62, 2323–2333.
- Charlou, J.L., Donval, J.P., Douville, E., Jean-Baptiste, P., Radford-Knoery, J., Fouquet, Y., Dapigny, A., Stievenard, M., 2000. Compared geochemical signatures and the evolution of Menez Gwen (37 degrees 50' N) and Lucky Strike (37 degrees 17' N) hydrothermal fluids, south of the Azores Triple Junction on the Mid-Atlantic Ridge. *Chemical Geology* 171, 49–75.
- Charlou, J.L., Donval, J.P., Fouquet, Y., Jean-Baptiste, P., Holm, N., 2002. Geochemistry of high H₂ and CH₄ vent fluids issuing from ultramafic rocks at the Rainbow hydrothermal field (36 degrees 14' N, MAR). *Chemical Geology* 191, 345–359.
- Cody, G.D., Bockor, N.Z., Brandes, J.A., Filley, T.R., Hazen, R.M., Yoder, H.S., 2004. Assaying the catalytic potential of transition metal sulfides for abiotic carbon fixation. *Geochimica et Cosmochimica Acta* 68, 2185.
- Drummond, S.E., 1981. Boiling and mixing of hydrothermal fluids: chemical effects on mineral precipitation.
- Emmanuel, S., Ague, J.J., 2007. Implications of present-day abiogenic methane fluxes for the early Archaean atmosphere. *Geophysical Research Letters* 34.
- Esteban, J.J., Cuevas, J., Tubia, J.M., Yusta, I., 2003. Xonotlite in rodingite assemblages from the Ronda peridotites, Betic Cordilleras, southern Spain. *The Canadian Mineralogist* 41, 161–170.
- Evans, B.W., 2008. Control of the products of serpentinization by the (FeMg)₁–Mg₂ exchange potential of olivine and orthopyroxene. *Journal Of Petrology* 49, 1873–1887.
- Fiebig, J., Woodland, A.B., Spangenberg, J., Oschmann, W., 2007. Natural evidence for rapid abiogenic hydrothermal generation of CH₄. *Geochimica et Cosmochimica Acta* 71, 3028–3039.
- Foustoukos, D.L., Seyfried, W.E., 2004. Hydrocarbons in hydrothermal vent fluids: the role of chromium-bearing catalysts. *Science* 304, 1002–1005.
- Frost, B.R., 1985. On the stability of sulfides, oxides, and native metals in serpentinite. *Journal Of Petrology* 26, 31–63.
- Fu, Q., Foustoukos, D.L., Seyfried Jr., W.E., 2008. Mineral catalyzed organic synthesis in hydrothermal systems: an experimental study using time-of-flight secondary ion mass spectrometry. *Geophysical Research Letters* 35.
- Ghiorso, M.S., Sack, R.O., 1995. Chemical mass-transfer in magmatic processes. 4. A revised and internally consistent thermodynamic model for the interpolation and extrapolation of liquid–solid equilibria in magmatic systems at elevated-temperatures and pressures. *Contributions To Mineralogy And Petrology* 119, 197–212.
- Godel, B., Barnes, S.J., 2008. Platinum-group elements in sulfide minerals and the whole rocks of the J-M Reef (Stillwater Complex): Implication for the formation of the reef. *Chemical Geology* 248, 272–294.
- Green, D.H., Ringwood, A.E., 1963. Mineral assemblages in a model mantle composition. *Journal Of Geophysical Research* 68, 937–945.
- Haqq-Misra, J.D., Domagal-Goldman, S.D., Kasting, P.J., Kasting, J.F., 2008. A revised, hazy methane greenhouse for the Archean Earth. *Astrobiology* 8, 1127–1137.
- Hoatson, D.M., Sun, S.S., Duggan, M.B., Davies, M.B., Daly, S.J., Purvis, A.C., 2005. Late Archean Lake Harris komatiite, central Gawler craton, South Australia: geologic setting and geochemistry. *Economic Geology* 100, 349–374.
- Horita, J., Berndt, M.E., 1999. Abiogenic methane formation and isotopic fractionation under hydrothermal conditions. *Science* 285, 1055–1057.
- Ingebritsen, S.E., Manning, C.E., 2002. Diffuse fluid flux through orogenic belts: implications for the world ocean. *Proceedings Of The National Academy Of Sciences Of The United States Of America*, v. 99, pp. 9113–9116.
- Jensen, L.S., 1976. A new cation plot for classifying subalkalic volcanic rocks.
- Johnson, J.W., Oelkers, E.H., Helgeson, H.C., 1992. SUPCRT92 — a software package for calculating the standard molal thermodynamic properties of minerals, gases, aqueous species, and reactions from 1-bar to 5000-bar and 0-degrees-C to 1000-degrees-C. *Computers and Geosciences* 18, 899–947.
- Kasting, J., 2005. Methane and climate during the Precambrian era. *Precambrian Research* 137, 119–129.
- Keays, R.R., 1995. The role of komatiitic and picritic magmatism and S-saturation in the formation of ore-deposits. *Lithos* 34, 1–18.
- Kelley, D.S., Karson, J.A., Fruh-Green, G.L., Yoergler, D.R., Shank, T.M., Butterfield, D.A., Hayes, J.M., Schrenk, M.O., Olson, E.J., Proskurowski, G., Jakuba, M., Bradley, A., Larson, B., Ludwig, K., Glickson, D., Buckman, K., Bradley, A.S., Brazelton, W.J., Roe, K., Elend, M.J., Delacour, A., Bernasconi, S.M., Lilley, M.D., Baross, J.A., Summons, R.E., Sylva, S.P., 2005. A serpentinite-hosted ecosystem: the Lost City hydrothermal field. *Science* 307, 1428–1434.
- Kinzler, R.J., Grove, T.L., 1985. Crystallization and differentiation of Archaean komatiite lavas from Northeast Ontario — phase-equilibrium and kinetic-studies. *American Mineralogist* 70, 40–51.
- Klein, F., Bach, W.G., 2009. Fe–Ni–Co–O–S phase relations in peridotite–seawater interactions. *Journal Of Petrology* 50, 37–59.
- Konhauser, K.O., Pecoits, E., Lalonde, S.V., Papineau, D., Nisbet, E.G., Barley, M.E., Arndt, N.T., Zahnle, K., Kamber, B.S., 2009. Oceanic nickel depletion and a methanogen famine before the Great Oxidation Event. *Nature* 458, 750–U85.
- Korenaga, J., 2003. Energetics of mantle convection and the fate of fossil heat. *Geophysical Research Letters* 30, 1437.
- Kress, M.E., McKay, C.P., 2004. Formation of methane in comet impacts: implications for Earth, Mars, and Titan. *Icarus* 168, 475–483.
- Lazar, C., Manning, C.E., Cody, G.D., and Davis, J.M., submitted for publication. A kinetic pressure effect on abiotic methanogenesis during water–rock interaction.
- Li, Z.X.A., Lee, C.T.A., 2006. Geochemical investigation of serpentinized oceanic lithospheric mantle in the Feather River Ophiolite, California: implications for the recycling rate of water by subduction. *Chemical Geology* 235, 161–185.
- Lorand, J.P., 1991. Sulphide petrology and sulphur geochemistry of orogenic lherzolites: a comparative study of the pyrenean bodies (France) and the Lanzo Massif (Italy). *Journal Of Petrology* 77–95.
- Lyons, J.R., Manning, C., Nimmo, F., 2005. Formation of methane on Mars by fluid–rock interaction in the crust. *Geophysical Research Letters* 32.
- Maclean, W.H., Shimazaki, H., 1976. Partition of Co, Ni, Cu, and Zn between sulfide and silicate liquids. *Economic Geology* 71, 1049–1057.
- Mavrogenes, J.A., O'Neill, H.S.C., 1999. The relative effects of pressure, temperature and oxygen fugacity on the solubility of sulfide in mafic magmas. *Geochimica et Cosmochimica Acta* 63, 1173–1180.
- McCollom, T.M., Seewald, J.S., 2001. A reassessment of the potential for reduction of dissolved CO₂ to hydrocarbons during serpentinization of olivine. *Geochimica et Cosmochimica Acta* 65, 3769–3778.
- McCollom, T.M., Seewald, J.S., 2003. Experimental constraints on the hydrothermal reactivity of organic acids and acid anions: I. Formic acid and formate. *Geochimica et Cosmochimica Acta* 67, 3625–3644.
- McCollom, T.M., Seewald, J.S., 2007. Abiotic synthesis of organic compounds in deep-sea hydrothermal environments. *Chemical Reviews* 107, 382.
- Nisbet, E.G., Fowler, C.M.R., 1983. Model for Archean plate-tectonics. *Geology* 11, 376–379.
- Pavlov, A.A., Kasting, J.F., Brown, L.L., Rages, K.A., Freedman, R., 2000. Greenhouse warming by CH₄ in the atmosphere of early Earth. *Journal Of Geophysical Research-Planets* 105, 11981–11990.
- Pavlov, A.A., Hurtgen, M.T., Kasting, J.F., Arthur, M.A., 2003. Methane-rich Proterozoic atmosphere? *Geology* 31, 87–90.
- Proskurowski, G., Lilley, M.D., Seewald, J.S., Fruh-Green, G.L., Olson, E.J., Lupton, J.E., Sylva, S.P., Kelley, D.S., 2008. Abiogenic hydrocarbon production at Lost City hydrothermal field. *Science* 319, 604–607.
- Pyke, D.R., Naldrett, A.J., Or, Eckstran, 1973. Archean ultramafic flows in Munro Township, Ontario. *Geological Society Of America Bulletin* 84, 955–977.
- Rye, R., Kuo, P.H., Holland, H.D., 1995. Atmospheric carbon dioxide concentrations before 2.2 billion years ago. *Nature* 378, 603–605.
- Sato, H., 1977. Nickel content of basaltic magmas: identification of primary magmas and a measure of the degree of olivine fractionation. *Lithos* 10, 113–120.
- Schmidt, M.W., Poli, S., 1998. Experimentally based water budgets for dehydrating slabs and consequences for arc magma generation. *Earth And Planetary Science Letters* 163, 361–379.
- Seward, T.M., Franck, E.U., 1981. The system hydrogen–water up to 440 degrees C and 2500 bar pressure. *Berichte der Bunsengesellschaft für Physikalische Chemie*.
- Seyfried, W.E.J., Janecky, D.R., Berndt, M.E., 1987. Rocking autoclaves for hydrothermal experiments II. The flexible reaction cell system. In: Barnes, H.L., Ulmer, G.C. (Eds.), *Hydrothermal Experimental Techniques*, Wiley Interscience, pp. 216–240.
- Sherwood Lollar, B., Westgate, T.D., Ward, J.A., Slater, G.F., Lacrampe-Couloume, G., 2002. Abiogenic formation of alkanes in the Earth's crust as a minor source for global hydrocarbon reservoirs. *Nature* 416, 522–524.
- Sleep, N.H., Windley, B.F., 1982. Archean plate-tectonics — constraints and inferences. *Journal Of Geology* 90, 363–379.
- Stone, W.E., Crocket, J.H., Fleet, M.E., 1996. Platinum-group mineral occurrence associated with flow top amygdale sulfides in komatiitic basalt, Abitibi Greenstone Belt, Ontario. *Mineralogy And Petrology* 56, 1–24.
- Tingle, T.N., Hochella, M.F., Becker, C.H., Malhotra, R., 1990. Organic compounds on crack surfaces in olivine from San Carlos, Arizona, and Hualalai volcano, Hawaii. *Geochimica et Cosmochimica Acta* 54, 477–485.
- Wetzel, L.R., Shock, E.L., 2000. Distinguishing ultramafic- from basalt-hosted submarine hydrothermal systems by comparing calculated vent fluid compositions. *Journal Of Geophysical Research-Solid Earth* 105, 8319–8340.
- Yoshizaki, M., Shibuya, T., Suzuki, K., Shimizu, K., Nakamura, K., Takai, K., Omori, S., Maruyama, S., 2009. H-2 generation by experimental hydrothermal alteration of komatiitic glass at 300 degrees C and 500 bars: a preliminary result from on-going experiment. *Geochemical Journal* 43, E17–E22.
- Yu, J.L., Savage, P.E., 1998. Decomposition of formic acid under hydrothermal conditions. *Industrial and Engineering Chemistry Research* 37, 2–10.